

Dynamic Estimation of Spin Spacecraft Based on Multiple-Station ISAR Images

Yejian Zhou^{ID}, Lei Zhang^{ID}, and Yunhe Cao

Abstract—Dynamic estimation of spin spacecraft is a challenge and plays a significant role in space situation awareness applications like potential space collision warning. Based on remote sensing technologies of laser and radar sensors, current methods almost adopt a match strategy to estimate the dynamic parameters of a particular target with the long-term measurement collection. These kinds of data-driven methods merely consider the inherent connection between the measured characters and target dynamic patterns, and can hardly be expanded to other spacecraft when the measurement collection is insufficient. Therefore, this article presents a novel approach to interpreting multiple-station inverse synthetic aperture radar (ISAR) images for the dynamic estimation of spin spacecraft. As a unique phenomenon of radar imaging, the imaging plane of ISAR observation not only depends on the change of the relative position between the target and radar, but also changes with the spin of the target. In order to decouple the target dynamic estimation from the determination of the imaging geometry, the angular diversity of multiple-station images is employed. The proposed algorithm deduces an explicit expression of target dynamic parameters under the imaging projection model of the multiple-station observation. By utilizing the chaotic grasshopper optimization algorithm (CGOA), it determines three crucial elements of the target spin motion with a two-step optimization, including instantaneous attitude, rotation shaft and rotation speed. Simulation experiments of a typical spin spacecraft, Tiangong-I (TG-I), illustrate the feasibility of the proposed method under different motion patterns.

Index Terms—Dynamic state estimation, image interpretation, multiple-station inverse synthetic aperture radar (ISAR) imaging, spin spacecraft.

I. INTRODUCTION

AS AN increasing number of spacecraft are launched into space, dynamic estimation of spin spacecraft has become an essential and challenging task in space situation awareness (SSA) applications. A typical application scenario is monitoring reenter events of some decommissioned spacecraft, like Tiangong-I (TG-I) [1]. Since it occupies a crowded

region of low earth orbiting (LEO) satellites, its dynamic information is of high importance to monitor its reenter event and avoid potential space collisions. Compared with commissioned spacecraft, decommissioned targets usually lose contact with the ground and their attitudes are no longer under control, yielding to a spin motion in the time-varying space environment [2], [3]. Therefore, it is inappropriate to estimate their spin motion analytically by the ego-motion estimation based on the measuring system mounted on board, such as the inertial navigation system and the global positioning system (GPS) [4], or the observation data conveyed from the target, like terrestrial images [5].

Reviewing relevant studies, the exterior measurement offers an alternative approach for estimating target spin motion with the accommodation of remote sensing technologies. For instance, the range measurements of the corner cube reflectors (CCRs) mounted on satellite targets were employed to determine their attitude in several references [6]–[9]. Organized by international laser ranging service (ILRS), global satellite laser ranging (SLR) stations dedicated to the continuous tracking of ENVISAT from 2013 to 2015 after the unexpected loss of contact had occurred [2]. The spin motion parameters, such as the target spin period and in-orbit attitude, were calculated by fitting the current measurement of the range residual (which was understood as the relative position of the CCR mounted on ENVISAT) with the historical database. Another typical method focuses on the manual matching of the observed 2-D radar imagery to the target 3-D model [3], [8]. In Germany, Fraunhofer FHR applied the tracking and imaging radar (TIRA) to generate 2-D inverse synthetic aperture radar (ISAR) imagery for dynamic estimation of ENVISAT from 2011 to 2017 [10]. The target attitude relative to a certain ISAR imaging plane can be determined by rotating the target 3-D model to match its projection on the imaging plane with the measured imagery. An engineering software tool was established, but it needed additional azimuth scaling in advance which is difficult to realize for spin targets. All in all, most approaches rely on long-term collections of the exterior measurement or prior image scaling information, and scarcely consider the parametric spin pattern of the target in the dynamic estimation. As a consequence, it is impracticable to estimate dynamic parameters of spin spacecraft in a data-driven manner when these prerequisites are limited (i.e., TG-I), which motivates the work in this article.

In order to get rid of these limitations, we explore the intrinsic connection between the target spin motion and acquired range-Doppler (RD) imagery, and present a novel algorithm

Manuscript received August 28, 2018; revised November 11, 2019; accepted December 8, 2019. Date of publication December 27, 2019; date of current version March 25, 2020. This work was supported in part by the National Natural Science Foundation of China under Grant 61771372 and Grant 61771367 and in part by the National Science Foundation of Shanghai under Grant 1428700. (Corresponding author: Lei Zhang.)

Y. Zhou and Y. Cao are with the National Laboratory of Radar Signal Processing, Xidian University, Xi'an 710071, China, and also with the Collaborative Innovation Center of Information Sensing and Understanding, Xidian University, Xi'an 710071, China.

L. Zhang is with the School of Electronics and Communication Engineering, Sun Yat-sen University, Guangzhou 510275, China (e-mail: zhanglei57@mail.sysu.edu.cn).

Color versions of one or more of the figures in this article are available online at <http://ieeexplore.ieee.org>.

Digital Object Identifier 10.1109/TGRS.2019.2959270

0196-2892 © 2019 IEEE. Personal use is permitted, but republication/redistribution requires IEEE permission.

See <https://www.ieee.org/publications/rights/index.html> for more information.

to estimate dynamic parameters of spin spacecraft based on multiple-station ISAR images. As a unique phenomenon of radar imaging, besides the change of the relative position between the target and radar, the spin of the target also decides the imaging plane of ISAR observation. In consequence, the scaling of the RD image fails when the imaging plane cannot be determined, and it makes the interpretation of the imagery even more difficult. In this article, the angular diversity of multiple-station images is employed to decouple the target dynamic estimation from the determination of the imaging geometry. Instead of the sequential processing strategy adopted in the motion estimation of attitude stabilized targets [11], [12], target instantaneous attitude is determined by the joint interpretation of the ranging information in the synchronous multiple-station images, where the ranging geometry depends only on the relative position between the target and radar. Then, the Doppler information of the synchronous multiple-station images is analytically investigated to estimate the spin parameters of the target.

A brief flow of the proposed method is given below. First, according to the target trajectory, a geometric model of the multiple-station ISAR observation is developed to calculate the radar line of sight (LOS) parameters of each radar station. Meanwhile, the dynamic model of the spacecraft is split into the trajectory and spin motion components in the imaging period of a single RD imagery. After that, an explicit expression is derived to bridge the dynamic parameters of target typical structures and their size features which are extracted from the acquired ISAR images. Based on this connection, the dynamic estimation of the spin spacecraft is converted to a two-step optimization, which is solved by the chaotic grasshopper optimization algorithm (CGOA) [13], [14]. Aiming at evaluating the accuracy of the target attitude and spin motion parameters in practical applications, a visual self-verification approach is also proposed through imagery reconstruction. Simulation experiments of TG-I demonstrate the feasibility and veracity of the proposed algorithm in four potential motion patterns, including precession, unstable precession, nutation and tumbling movement, which are concluded from the observations of ENVISAT in practical applications [2], [3], [9], [10], [15].

Compared with the existing methods, the proposed algorithm has some innovations which are as follows.

- 1) To the best of our knowledge, it is the first time that the dynamic parameters of a spin spacecraft have been determined without the dependence of long-term observation collections or a complete simulation database. Different from the conventional methods, it can be executed independently in each observation of most spin targets if their structural knowledge is acquired in advance. Therefore, the proposed algorithm offers the possibility of accessing the dynamic monitoring for spin spacecraft when their motion patterns consistently change in the time-varying space environment.
- 2) Another contribution is designing a framework of the multiple-station ISAR observation for the sake of spacecraft dynamic analysis. The multiple-station cooperation strategy makes up for the angular limitation of the

single-station observation and is beneficial to mining the elementary geometrical information of the ISAR imaging observation to make deep interpretations of the radar imagery. This method is advantageous in that it not only avoids information loss brought by the angular glint phenomenon in the single-station image, but also has the potential of the multiple-band applications.

- 3) The self-verification method proposed in this article provides an essential approach to evaluating the estimation result of the target motion state. Most current algorithms are demonstrated with the internal control parameters of cooperative targets or the long-term statistics of noncooperative targets, whereas the estimation results can be verified with a comparison between the original imagery and reconstructed imagery readily in this article. With the great development of remote sensing technologies, it can be applied to various applications for which the accuracy and visualization of dynamic estimation constitute elementary requirements.

The remainder of this article is organized as follows. Section II introduces the fundamental of the proposed algorithm, where the imaging geometry of the multiple-station ISAR observation is developed. Combined with the dynamic model of the spacecraft, it is utilized to derive an explicit expression to connect target dynamic parameters and ISAR images. Section III describes the dynamic estimation approach with four detailed steps, including RD image acquisition, image feature extraction, target dynamic estimation, and result self-verification. Section IV demonstrates the feasibility of the proposed algorithm in different motion patterns, which are concluded from the relevant observations of ENVISAT. Some crucial conclusions of this article are drawn in Section V.

II. FUNDAMENTALS OF TARGET DYNAMIC ESTIMATION

In this section, the fundamentals of the proposed algorithm are introduced. The geometric model of the multiple-station ISAR observation framework and the dynamic model of spin spacecraft are developed in the first two subsections. Based on them, a deep interpretation of the RD imagery is investigated in the third subsection, where some image features are related to the target spin motion with an explicit expression.

A. Imaging Geometry of the Multiple-Station ISAR Observation Framework

The imaging geometry of the multiple-station ISAR observation framework is depicted in Fig. 1. During the passing of a spacecraft over ground radar stations, the target is projected with different poses on different imaging planes. In order to uniformly express the target motions in a certain coordinate system, the target Cartesian coordinate system is established to describe all target dynamic parameters in this article, as shown in Fig. 2. The target Cartesian coordinate system is defined as below: X -axis always points near the Earth's core, Y -axis is tangent to the target orbit and consistent with the direction of the target trajectory motion, and Z -axis is the normal direction of the target trajectory plane. As shown in Fig. 1, the trajectory motion of the spacecraft gives rise to the relative

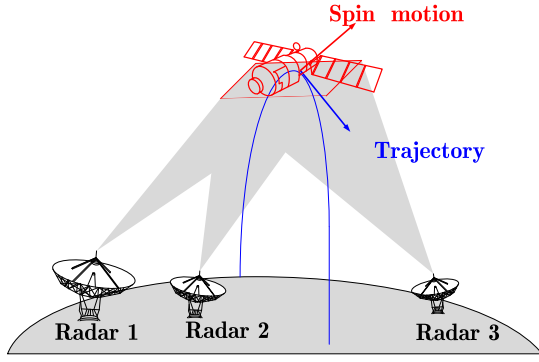


Fig. 1. Imaging geometry of the multiple-station ISAR observation framework.

rotation between the target and the ground radar. When the position of the spacecraft is fixed in the target Cartesian coordinates, the relative rotation is uniquely determined by the change of the radar LOS parameters, which coincides with the classical turn-table model. Furthermore, instantaneous radar sight direction \vec{k} is defined as a vector centered at the target position and oriented toward the ground radar station, which is represented by LOS parameters, elevation angle θ , and azimuth angle ϕ , as in

$$\vec{k} = (\cos \theta(t_m) \sin \phi(t_m), \cos \theta(t_m) \cos \phi(t_m), \sin \theta(t_m))^T \quad (1)$$

where t_m denotes the slow-time relative to the sampling in the azimuth direction, elevation angle $\theta(t_m)$ is the intersection angle between instantaneous radar LOS vector and the XOY -plane, and azimuth angle $\phi(t_m)$ is the intersection angle between Y -axis and the projection of instantaneous radar LOS vector in the XOY -plane.

In this article, the LOS sequence acquirement is based on an assumption that the space target is in a stabilized Keplerian orbit. It means two line ephemeris (TLE) parameters can be directly applied to determine the target position in the simplified general perturbation (SGP-4) model. After synchronizing GPS time with the reference time broadcast in TLE parameters, LOS parameter sequences are calculated with the longitude, latitude, and altitude of radar stations. The detailed computation is introduced in relevant references [16], [17]. In practical applications, the azimuth angle and elevation angle are loaded from the radar tracking system. After atmosphere correction and time synchronization, the multiple-station tracking data are analyzed jointly to determine the instantaneous radar sight direction of each station [18].

B. Spin Motion Model During the Single Imaging Period

The spin motion model is developed to describe the rotation of spin spacecraft during the single imaging period. An assumption is made that it rotates around a certain rotation shaft with a constant speed. And the different spin patterns are simulated by the change of the rotation shaft and speed. From relevant researches of ENVISAT [9], [10], the spin period of spacecraft is almost at the 160-s magnitude. When taking the trajectory motion of LEO targets (like ENVISAT

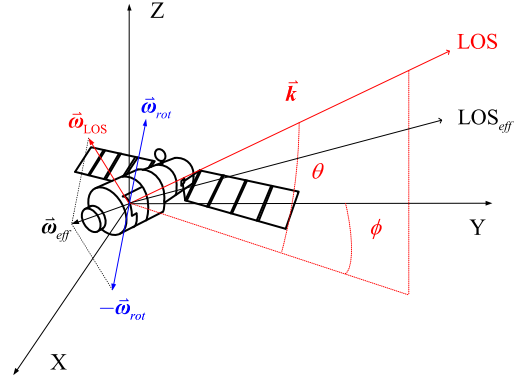


Fig. 2. Spin motion model of uncontrolled spacecraft.

and TG-I) into consideration, the single imaging period is reckoned at several seconds. Therefore, this spin motion model is acceptable for instantaneous spin motion estimation. In this article, the continuous estimation result under this motion model can be applied to express the dynamic estimation of the spacecraft.

As depicted in Fig. 2, the spin component of the target is represented with a vector, namely

$$\vec{w}_{\text{rot}} = (\cos \theta_{\text{rot}} \sin \phi_{\text{rot}}, \cos \theta_{\text{rot}} \cos \phi_{\text{rot}}, \sin \theta_{\text{rot}})^T \omega_{\text{rot}} \quad (2)$$

where θ_{rot} and ϕ_{rot} are directional parameters of the rotation shaft, which are defined in the same way as LOS parameters, and ω_{rot} is the rotation speed.

During the single imaging period, the relative motion of a certain scattering point on the target to the ground radar is composed of the change of view angle \vec{w}_{LOS} and the target spin motion \vec{w}_{rot} . The change component of view angle is caused by the target trajectory and can be calculated with the LOS sequence which is acquired in the previous subsection. It is crucial to point out that the direction of \vec{w}_{LOS} is determined by the start LOS vector and the end LOS vector of the current image according to the right-hand principle, and the angular speed is equal to the intersection angle of these two vectors divided by the imaging time. The calculation of the view angle component is sufficient to determine the imaging geometry for attitude stabilized targets, which is explored in various practical applications [5], [19], whereas the target spin component is unknown and changes the imaging geometry for spin targets.

In order to decouple the target dynamic estimation from the determination of the imaging geometry, we assume that the target is attitude stabilized during the imaging period. The relative motion component caused by the target spin can be replaced by the coaxial reverse rotation of the target (i.e., $-\vec{w}_{\text{rot}}$). In this way, the target-to-radar relative motion will be interpreted as the target is attitude stabilized while the equivalent radar LOS \vec{w}_{eff} , which synthesizes the target spin motion and the target trajectory, determines the imaging plane of the ISAR observation

$$\vec{w}_{\text{eff}} = \vec{w}_{\text{LOS}} - \vec{w}_{\text{rot}}. \quad (3)$$

It should be particularly noted that all dynamic parameters correspond to the center moment of the single imaging period.

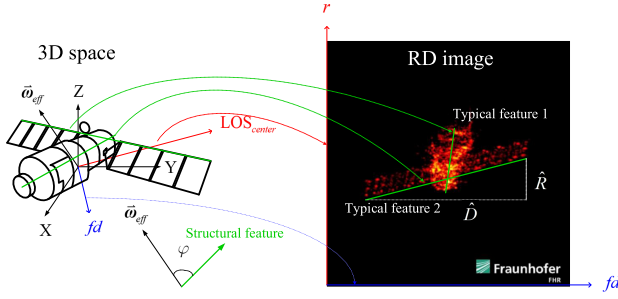


Fig. 3. Imagery interpretation in the ISAR imaging projection theory.

When the center moment is considered as the reference time, the spin accumulation of this moment is zero. That is to say, when and only when at the reference time, the instantaneous equivalent radar LOS does not have the contribution of the target spin component, which totally depends on the relative position between the target and ground radar. A simple conclusion can be drawn that the range direction in the RD image does not change under this motion model.

C. Dynamic Estimation of Spin Spacecraft From Multiple-Station ISAR Images

In this section, how to employ the multiple-station ISAR images to estimate the target attitude and spin parameters is discussed. According to the ISAR imaging projection theory [20], ISAR imaging for space targets can be understood as the geometric projection of the scattering centers on the radar imaging plane. In this article, it is extended as the range dimension information of the pixels in the imagery is the distance measurement of each scattering center while the Doppler dimension information of the pixels reflects the relative rotation of each scattering center. Supported by ISAR imaging geometry and the Doppler principle, this understanding helps us determine the target dynamic parameters from ISAR images when the knowledge of target sizes is provided in advance. In brief, given the prior target sizes, the range dimension information of multiple-station ISAR images is utilized to determine the target attitude while the Doppler dimension information of multiple-station ISAR images is employed to estimate the spin parameters of the target. Detailed derivations are presented below. Take TG-I for example. As shown in Fig. 3, it is projected as two typical structural features, the spacecraft body and the solar wing, in an RD imagery. The projection length of a typical structural feature on the range axis can be expressed as

$$R = \left| \vec{k}_{center} \cdot \vec{1} \right| L \quad (4)$$

$$\vec{1} = (\cos \alpha \sin \beta, \cos \alpha \cos \beta, \sin \alpha)^T \quad (5)$$

where α and β represent attitude parameters of the typical structure, which are defined in the same way as LOS parameters, $|\cdot|$ indicates modulus operation, L refers to the prior 3-D length of the typical structure, \cdot denotes the inner product, and \vec{k}_{center} is the center LOS vector of the imagery.

In view of line equations, we only need to establish two-station observation equations for solving binary parameters (α and β). However, when the equation manifold is taken into account, it is necessary to set up an overdetermined system of equations aiming at reducing the impact of the extraction bias of the projection length. The proposed algorithm takes three-station observation for reference, namely

$$\begin{cases} R_1 = \left| \vec{k}_{center,1} \cdot \vec{1} \right| \\ R_2 = \left| \vec{k}_{center,2} \cdot \vec{1} \right| \\ R_3 = \left| \vec{k}_{center,3} \cdot \vec{1} \right| \end{cases} \quad (6)$$

The observation (6) can be established for each typical structure independently. Furthermore, with the accommodation of the prior orthogonality constraint between typical structure 1 and typical structure 2, the joint attitude estimation of two typical structures is converted to optimization (7), as shown at the bottom of this page, where $\hat{R}_{1,j}$ and $\hat{R}_{2,j}$ represent the range size extraction results of a typical structure 1 and typical structure 2 in the imagery, respectively, j refers to the number of radar stations, and a_1 is a balance actor. The optimal selection of a_1 depends on the extraction precision of typical structures in the imagery, which contributes to the accuracy of the attitude estimation.

Optimization (7) can be solved in various ways. In this article, CGOA is adopted to estimate the attitude parameters of each typical structure. The details are given in Section III-C. With the optimal $(\tilde{\alpha}_1, \tilde{\beta}_1, \tilde{\alpha}_2, \tilde{\beta}_2)^T$, the attitude vectors of typical structures can be calculated according to (5)

$$\vec{1}_1 = (\cos \tilde{\alpha}_1 \sin \tilde{\beta}_1, \cos \tilde{\alpha}_1 \cos \tilde{\beta}_1, \sin \tilde{\alpha}_1)^T \quad (8)$$

$$\vec{1}_2 = (\cos \tilde{\alpha}_2 \sin \tilde{\beta}_2, \cos \tilde{\alpha}_2 \cos \tilde{\beta}_2, \sin \tilde{\alpha}_2)^T \quad (9)$$

Attitude vectors of typical structures are applied directly to determine the rotation shaft and speed in a similar way. According to (2) and (3), the equivalent radar LOS \vec{w}_{eff} can be utilized to determine the spatial Doppler direction in the manner

$$\vec{fd} = \frac{\vec{k}_{center} \times \vec{w}_{eff}}{\left\| \vec{k}_{center} \times \vec{w}_{eff} \right\|} \quad (10)$$

where \times indicates the cross product, and $\|\cdot\|$ refers to the modulus of a vector.

$$\begin{aligned} \min_{\alpha_1, \alpha_2, \beta_1, \beta_2} & \sum_{j=1}^3 \left(\left| \vec{k}_{center,j} \cdot \vec{1}_1 \right| - \hat{R}_{1,j} \right)^2 + a_1 \left(\left| \vec{k}_{center,j} \cdot \vec{1}_2 \right| - \hat{R}_{2,j} \right)^2 \\ s.t. & \tan \alpha_1 \tan \alpha_2 + \cos (\beta_1 - \beta_2) = 0 \end{aligned} \quad (7)$$

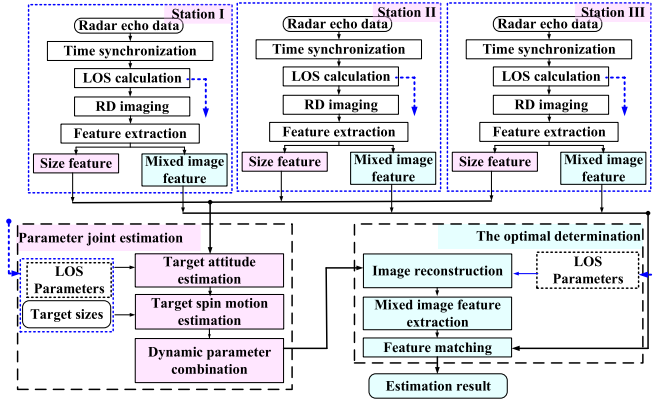


Fig. 4. Flowchart of the proposed algorithm.

Here, the projection length of a typical feature on the Doppler direction can be expressed as

$$d = \left| \vec{fd} \cdot \vec{1} \right| L_{\text{eff}} \sin \varphi \quad (11)$$

$$\sin \varphi = \sqrt{1 - \left(\vec{fd} \cdot \vec{1} \right)^2} \quad (12)$$

where φ is the intersection angle between the rotation shaft and the attitude vector of the typical structure as shown in Fig. 2.

Similar to the attitude optimization (7), the target spin state optimization is expressed as

$$\min_{\theta_{\text{rot}}, \phi_{\text{rot}}, \omega_{\text{rot}}} \sum_{j=1}^3 \left(d_{1,j} - \hat{D}_{1,j} \right)^2 + a_2 \left(d_{2,j} - \hat{D}_{2,j} \right)^2 \quad (13)$$

where $\hat{D}_{1,j}$ and $\hat{D}_{2,j}$ represent Doppler size extraction of typical structure 1 and typical structure 2 in the imagery, respectively, j refers to the number of radars, and a_2 is a balance factor.

III. THREE-STATION ALGORITHM OF THE TARGET DYNAMIC ESTIMATION

The dynamic estimation of spin spacecraft comprises four components: RD image acquisition, image feature extraction, target dynamic estimation, and result self-verification. The flow of the proposed method is depicted in Fig. 4, and the detailed steps are as follows.

- 1) *Step 1*: For the obtained three-station radar data, the time synchronization is executed according to the method mentioned in Section II-A.
- 2) *Step 2*: The LOS sequence of each station is calculated to determine the radar observation geometry. Then, the synchronous echo data are processed with the RD algorithm to generate three synchronous RD images.
- 3) *Step 3*: The target size feature and mixed image features are extracted from RD images. The target size feature is obtained through manual measurement of the projection lengths of typical structures in RD images, whereas Radon transform and multiscale Gabor filter groups are adopted to extract the mixed image features automatically.

- 4) *Step 4*: Combined with three-station LOS sequences, the extracted range information is substituted into optimization (7) to estimate the instantaneous target attitude.
- 5) *Step 5*: With the accommodation of the attitude estimation result, the extracted Doppler information is substituted into optimization (13) to determine the rotation shaft and speed of the target.
- 6) *Step 6*: According to Steps 4 and 5, the target state information is obtained, and a set of alternative reconstruction images are generated via the RD image simulation method.
- 7) *Step 7*: Mixed image features of each reconstructed result are extracted to determine the unique reconstructed image by matching them to mixed image features of the original observed image, which is extracted in Step 3. In the end, the accuracy of the estimation is verified with a visual comparison.

The key steps of the proposed approach are discussed as follows.

A. Acquisition of RD Imagery

The synchronization of the multiple-station observation is an important prerequisite for the proposed algorithm. A 0.01-s synchronization accuracy is required for this task which can be guaranteed in most practical observations. After the synchronization is completed, the observation geometry between the target and radar stations is determined. It is utilized to calculate the LOS changing component \vec{w}_{LOS} due to the target trajectory in (3). Meanwhile, the manifold of the multiple-station observation matrix \mathbf{A} can also be calculated with the observation geometry

$$\mathbf{A} = \begin{bmatrix} \vec{k}_{\text{center},1}^T \\ \vec{k}_{\text{center},2}^T \\ \vec{k}_{\text{center},3}^T \end{bmatrix} \quad (14)$$

$$\kappa(\mathbf{A}) = \frac{\max \frac{\|\mathbf{A}x\|}{\|x\|}}{\min \frac{\|\mathbf{A}x\|}{\|x\|}} \quad (15)$$

where $\kappa(\mathbf{A})$ refers to the matrix condition number, which can be obtained by the singular value decomposition (SVD) algorithm to determine the solution reliability of the optimization (7). In general, it ought to be less than 500 for practical tasks, which puts forward the requirement of the radar distribution in the multiple-station observation framework.

In practical observations, RD imaging for satellite targets is divided into several stages including translation motion compensation, range compression, and azimuth compression [21]. Since the trajectory of LEO space targets is relatively stable and brings up a sufficient turn speed to the ground radar, high-resolution capability of ISAR imaging can be guaranteed by compressive sensing and other technologies [22], [23]. Different from the conventional imaging flow, this article preserves the Doppler information of the imagery and does not convey it to the length information with the azimuth scaling. The reason is that for the lack of knowledge of the target spin pattern, the angular accumulation of the single imaging period

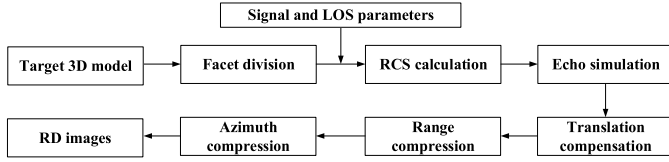


Fig. 5. Brief flow of the RD image simulation.

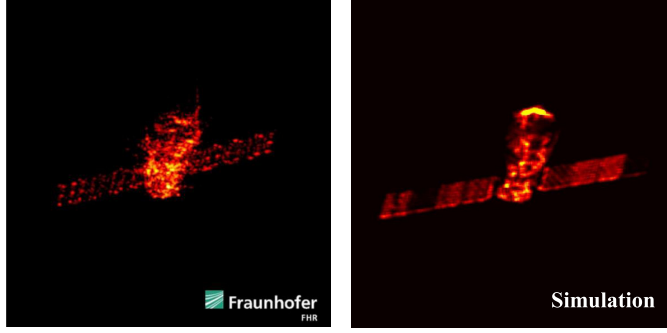


Fig. 6. Visual comparison between the simulated imagery and the measured RD imagery.

cannot be calculated. The resolutions of acquired RD imagery are expressed as

$$\Delta r = c/2f_s \quad (16)$$

$$\Delta f_a = \lambda/2\Delta T \quad (17)$$

where f_s is the radar sampling frequency, ΔT refers to the time accumulation of the current image, λ represents the signal wavelength, and c denotes the speed of light.

Due to the limitation of the real-measured ISAR data for public use, the proposed algorithm is investigated with simulation imagery. All simulations adopt a triangular facet model to divide the target surface into thousands of equivalent scatterers [24], [25]. The radar cross section (RCS) of each scatterer depends on the area of the triangle, the signal frequency, and the incidence angle. The radar echo data of a solid object is calculated by adopting the fast physical optics (FPO) algorithm [26]. Then, the simulated RD image is generated by the RD imaging algorithm [21]. The brief flow of the RD image simulation is depicted in Fig. 5. A visual comparison between a simulated image and a measured RD image is given in Fig. 6. The measurement image was published by the German FGAN Lab in March, 2018 (at Fraunhofer FHR) [27]. From the comparison result, it can be noted that the performance of the generated imagery is close to that of the measured ISAR image, which supports the investigation in this article.

B. Extraction of Image Features

In this article, the features extracted from the RD imagery include two types: target size feature in the RD image which

is used to estimate the target motion state, and mixed image features which are adopted as matching features to determine the unique reconstructed image. The extraction technologies are as follows.

- 1) *The extraction of size feature:* The size feature of typical structures is extracted manually in RD imagery. The veracity of size extraction will directly impact the accuracy of target state analysis, which is quantified in the experimental part. In practical applications, it is an effective approach to applying background segmentation, polygon fitting, morphological processing, and other relevant image processing techniques to achieve the automatic size extraction [28].
- 2) *The extraction of mixed image features:* Mixed image features include image structure feature and image texture feature. Image structure feature describes the structural distribution of strong scatterers in the image, and is obtained via performing entire image with the Radon transform [29]. It is understood as the projection integral of target pixels in a certain orientation of the RD imagery. Although the centroid of the target shifts in the simulation image, the transformation result reflects the target structural information in the imagery to some degree. The other feature, image texture feature, is extracted by a set of Gabor filter groups [30], [31]. It is designed as the secondary feature to describe the texture differentiation among images. Empirically, this article utilizes a Gabor filter group with scales of 3, 10, 15, and 50 pixels to extract the texture feature of a 512×512 image.

C. Optimization Technique of the Target Dynamic Estimation

The grasshopper optimization algorithm (GOA) is a stochastic intelligent algorithm. Inspired by the food-seeking behavior of grasshoppers, it is widely applied to search the optima [13], [32]. As a stochastic intelligent algorithm, it implements the global search with random steps and will be trapped in a local optima in some cases. Some boosting studies are presented by employing the chaotic theory into GOA to accelerate its global convergence speed and prevent it from being trapped into a local optimum [14].

In this article, CGOA is adopted to solve the attitude optimization (7) and spin motion optimization (13). The solution of optimization (7) is defined as the particle position in CGOA

$$X_i = (\alpha_1, \beta_1, \alpha_2, \beta_2)^T. \quad (18)$$

With the prior orthogonality restriction of the typical structures 1 and 2, the fitness function of optimization (7) is defined as (19), as shown at the bottom of this page, where the confidence factor a_3 is uniformly distributed within $[0, 1]$, which ensures the orthogonality restriction. Empirically, it is set to be 0.95 in this article.

$$J = \sum_{j=1}^3 \left(\left| \vec{k}_{center,j} \cdot \vec{l}_1 \right| - R_{1,j} \right)^2 + a_1 \left(\left| \vec{k}_{center,j} \cdot \vec{l}_2 \right| - R_{2,j} \right)^2 + a_3 |\tan \alpha_1 \tan \alpha_2 + \cos(\beta_1 - \beta_2)| \quad (19)$$

During the process of CGOA, the food-seeking strategy consists of exploration and exploitation tendencies. In the exploration stage, the particle moves toward the best one which has the nearest position to the food, while the movement of the particle depends on its position in the swarm during the exploitation period. The classical updating rule is adopted as follows:

$$X_i = c_1(t) \left(\sum_{j=1, j \neq i}^N c_2(t) s(|\vec{d}_{i,j}|) \frac{\vec{d}_{i,j}}{|\vec{d}_{i,j}|} \right) + X_{best} \quad (20)$$

where $\vec{d}_{i,j}$ refers to the pointing vector between the i th particle and the j th particle, X_{best} is the current best particle position, and the swarm interaction is defined as

$$s(|\vec{d}_{i,j}|) = f e^{\frac{|\vec{d}_{i,j}|}{l}} - e^{-|\vec{d}_{i,j}|} \quad (21)$$

where f indicates the attractive intensity, and l refers to the attractive length.

The parameter $c_1(t)$ is utilized to balance the exploration and the exploitation contributions, whereas the parameter $c_2(t)$ decreases attraction zone, comfort zone, and repulsion zone during the updating iteration. Different from the classical GOA, these two crucial parameters are generated through chaotic maps to improve the optimization performance in CGOA. In this article, the circle map, a member of dynamical systems on circle, is adopted [33]

$$c(t+1) = \left(c(t) + b - \frac{P}{2\pi} \sin(2\pi c(t)) \right) \bmod(1) \quad (22)$$

where the control parameters P and b are equal to 0.5 and 0.2, respectively.

A brief flow of CGOA is given as follows.

- 1) *Step 1*: Set the minimum move distance. Generate a particle swarm by random sampling of the solution space of the optimization.
- 2) *Step 2*: Search the best particle $c_1(t)$ and $c_2(t)$ with the fitness function in the swarm.
- 3) *Step 3*: Update parameters $c_1(t)$ and $c_2(t)$ according to (22).
- 4) *Step 4*: Move each particle position according to (20), and search the new best particle X'_{best} . Then, calculate the move distance between X_{best} and X'_{best} . If the maximum iterations or minimum move criterion of the best position is satisfied, break the current iteration and turn to Step 5; otherwise, turn to Step 3.
- 5) *Step 5*: Output the position of the ideal particle \tilde{X} .

Similar to optimization (7), the solution of optimization (13) is defined as the particle position in CGOA

$$X_i = (\theta_{rot}, \phi_{rot}, \omega_{rot})^T. \quad (23)$$

And optimization (13) is converted to the fitness as

$$J = \sum_{j=1}^3 (d_{1,j} - D_{1,j})^2 + a_2 (d_{2,j} - D_{2,j})^2 \quad (24)$$

$$d_{i,j} = \left| \vec{f} \vec{d}_j \cdot \vec{1}_i \right| L \omega_{eff} \sqrt{1 - \left(\vec{f} \vec{d}_j \cdot \vec{1}_i \right)^2}. \quad (25)$$

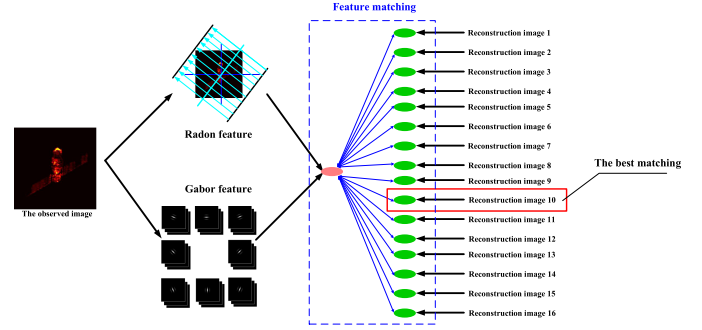


Fig. 7. Diagram of the unique reconstructed image determination.

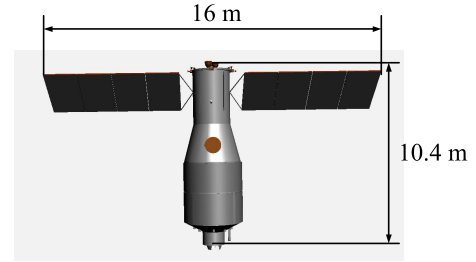


Fig. 8. 3-D model of TG-I Spacecraft.

D. Self-Verification of the Estimation Result

In order to evaluate the accuracy of the target attitude and rotation parameters in practical applications, an image reconstruction approach is proposed based on the target 3-D model. The estimated target rotation parameters is applied to synthesize an effective LOS sequence through the method in Section II-A. Meanwhile, the estimated target attitude parameters are adopted to rotate the target 3-D model into a definite pose. The radar echo is calculated by the simulation method in Section III-A and is utilized to reconstruct RD images by the RD imaging algorithm.

It needs to be noted that a set of target dynamic parameters will generate 16 alternative images due to the modulus operations adopted in the two-step optimization of target dynamic parameters. The reasons are as follows: for a group of target attitude parameters $(\alpha_1, \beta_1, \alpha_2, \beta_2)^T$, there are four groups of rotation modes when the positive and negative directions of the estimated attitude vector are taken into consideration. Similarly, there are two types of target spin modes corresponding to one set of target rotation speed parameters, and both positive and negative directions of the distance measurement correspond to a definite LOS vector. Theoretically, the modulus operations are dispensable and can be replaced by the uniform regulation of the size feature extraction direction. However, this extraction regulation will make the size feature extraction even more complicated in practical tasks. Therefore, although the modulus operation brings about a multiple-solution condition, it ensures the practicality of the proposed algorithm and is retained. By contrast, with the accommodation of mixed image features, a matching approach is presented to determine the unique reconstruction image corresponding to the original

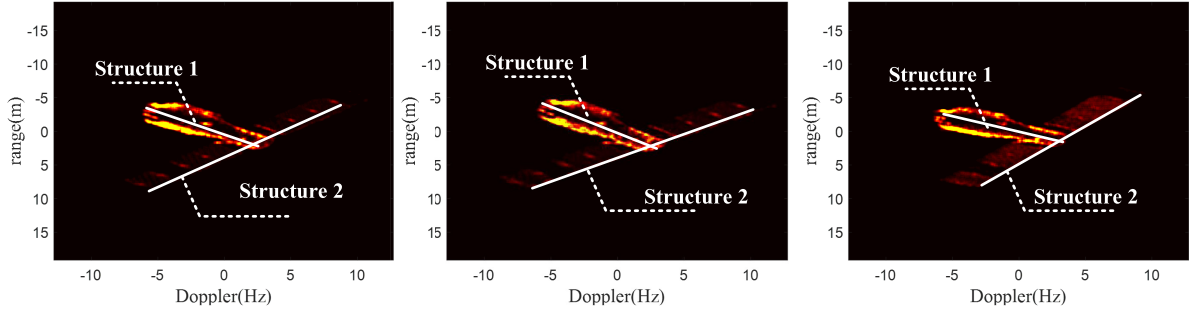


Fig. 9. Synchronous RD imagery of TG-I at a certain moment.

observation. A diagram is depicted of the unique reconstructed image determination as in Fig. 7.

The feature matching relies on the Gabor texture and Radon orientation features of RD images. The matching cost function is defined as

$$J(i) = Cor(\vec{T}_{G,original}, \vec{T}_{G,i}) + a_4 Cor(\vec{T}_{R,original}, \vec{T}_{R,i}) \quad (26)$$

where $\vec{T}_{G,*}$ refers to the Gabor texture feature vector of the imagery, whereas $\vec{T}_{R,*}$ refers to the Radon orientation feature vector of the imagery, $Cor(*,*)$ indicates the correlation between two feature vectors, the subscript original denotes the original observation image, whereas the subscript i is the number of alternative reconstruction images, and weight actor a_4 balances the contributions of these two features in feature matching and is set within [2, 4] empirically.

The unique reconstructed image reflects the reliability of the estimation intuitively after visual comparison with the original image. However, for most in-orbit spacecraft, quantitative comparisons between the target attitude and spin parameters are still difficult to be made in practical observations.

IV. EXPERIMENTAL ANALYSIS

As the real-data of spin in-orbit satellites is not publically accessible, the feasibility and veracity of the proposed algorithm will be assessed by three simulation experiments in this article. The details are as follows.

- 1) First of all, the dynamic parameters of a typical target, TG-I, are estimated by the proposed algorithm based on three synchronous ISAR images.
- 2) Secondly, the estimation error caused by the extraction of size features is analyzed.
- 3) Drawing on the observation experience of ENVISAT, the proposed algorithm is tested in four target spin patterns to prove its feasibility for practical tasks in the third experiment.

The 3-D model of TG-I is depicted in Fig. 8. The geographical coordinates of three radar stations are listed in Table I, and the main parameters of the radar system are given in Table II. The target TLE parameters are based on a set of public data, according to which the orbit altitude of TG-I was at around 400 km in 2016. Supported by Satellite Tool Kit (STK)

TABLE I
GEOGRAPHICAL COORDINATES OF THREE RADAR STATIONS

Radar Station	Location
Beijing	(39.9 N, 116.4 E, 88 m)
Tianjin	(39.1 N, 117.2 E, 0 m)
Shijiazhuang	(38.0 N, 114.5 E, 0 m)

TABLE II
MAIN PARAMETERS OF THE RADAR SYSTEM

Parameters	Value
Size of a Single Image	512 × 512
Wavelength	0.03 m
Bandwidth	1 GHz
Signal Frequency	10 GHz
Pulse Repetition Frequency	100 Hz

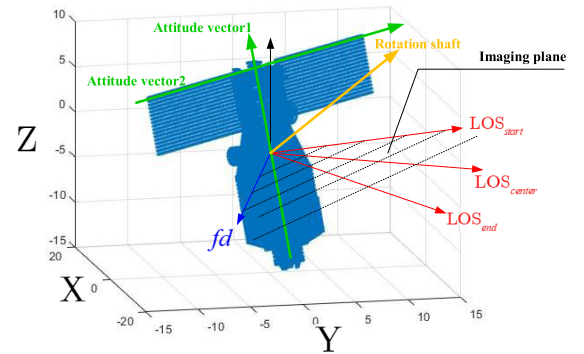


Fig. 10. Visual estimation results in the target Cartesian coordinates.

simulation, the observation of distributed ISAR configurations is guaranteed within the visual scope. The acquirement of the simulation imagery is introduced in Section III-A, where the comparison with the measured ISAR imagery published by the FGAN Lab is also made. The signal-to-noise ratio (SNR) of each RD image is set to be 10 dB.

A. Instantaneous Estimation of TG-I

Three synchronous RD images of TG-I at a certain moment are presented in Fig. 9. During the imaging period, TG-I

TABLE III
STATE ESTIMATION RESULT OF TG-I

	Estimation Value	True Value	Error
Body Attitude	(0.1098,-0.0888,-0.9900)	(-0.1330,0.1116,0.9848)	1.8879 degrees
Solar Wings Attitude	(0.6495,0.7603,0.0039)	(0.6428,0.7660,-0.0000)	0.5531 degrees
Rotation Shaft	(0.9991,0.0420,0.0101)	(1.0000,0.0000,0.0000)	2.4310 degrees
Rotation Speed	0.0153 rad/s	0.0150 rad/s	0.0003 rad/s

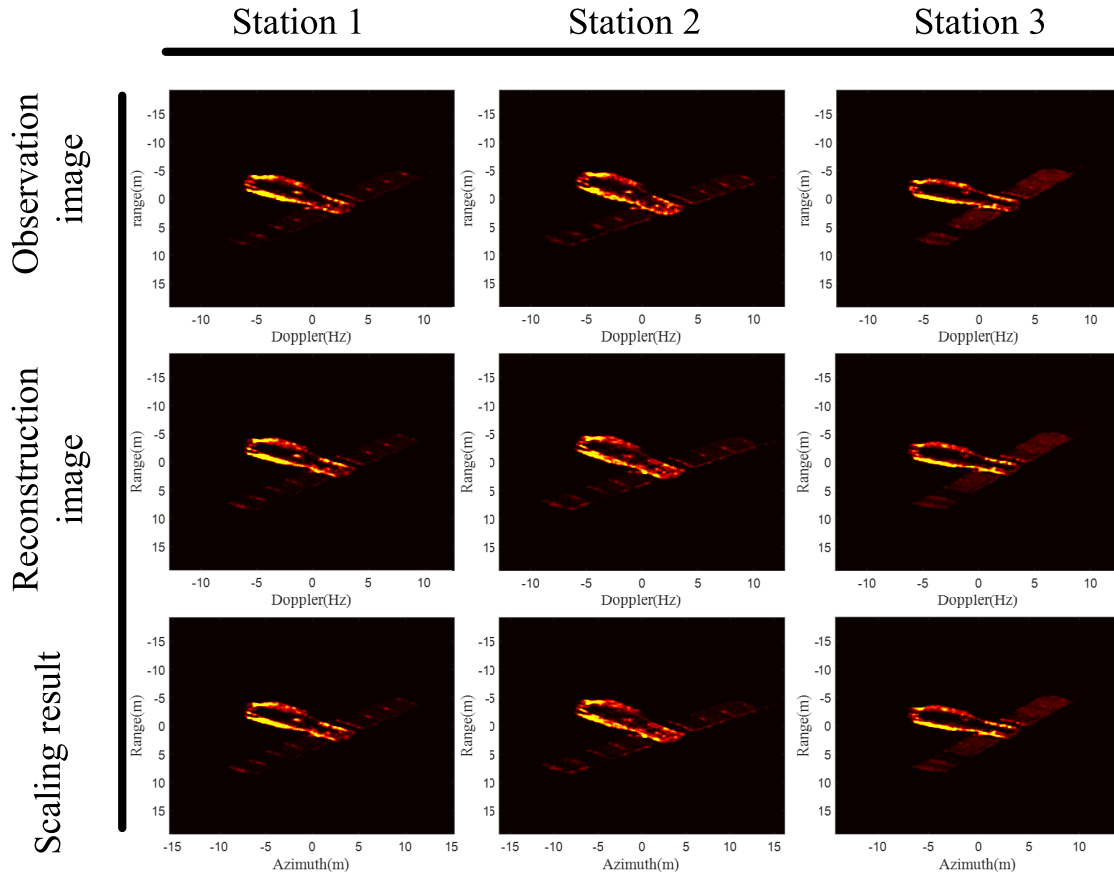


Fig. 11. Visual estimation results of TG-I.

spacecraft is set to spin around a certain shaft at a constant rotation speed. The size feature extraction result of two typical components, the spacecraft body and the solar wing, is marked white in Fig. 9, and is applied to estimate the target attitude in optimization (7). After that, combined with the Doppler information of the size feature extraction, the attitude estimation result is substituted into optimization (13) to estimate the rotation shaft and rotation speed of TG-I. The numerical comparison between the estimation results and true values is listed in Table III, and a visual estimation result is given in Fig. 10. As can be seen, the numerical estimation results are close to the true values, which demonstrate the veracity of the proposed algorithm.

As mentioned above, we combine the estimation result with the observation geometry to provide three reconstruction images in this case for self-verification of the estimation reliability. The visual comparison between the observed image

and the reconstruction image is given in the first and second rows of Fig. 11. The projection poses of TG-I are semblable in these two image groups, and only slight rotation appears in the reconstruction images due to estimation bias. When the target spin parameters are acquired, azimuth scaling is available as given in the third row of Fig. 11.

B. Performance Investigation

In this article, both attitude optimization and spin state optimization are based on the size feature of typical structures extracted from the RD imagery. The extraction precision of the size feature is the major factor affecting the accuracy of the target state estimation. In order to investigate the sensitivity of the proposed algorithm against the size feature extraction error, the target state estimation experiment is repeated indifferent conditions of size feature extraction. The proposed algorithm is

TABLE IV
ESTIMATION RESULTS OF THE PRECESSION

Observation Time	Estimation Error of the Body	Estimation Error of the Solar Wing	Estimation Error of the Rotation Shaft	True value of the Rotation Speed	Estimation of the Rotation Speed
Time 1	1.0573 degrees	1.4451 degrees	0.7845 degrees	0.0150(rad/s)	0.0155(rad/s)
Time 2	1.1410 degrees	1.4201 degrees	1.7955 degrees	0.0150(rad/s)	0.0157(rad/s)
Time 3	1.4123 degrees	1.3013 degrees	4.1839 degrees	0.0150(rad/s)	0.0162(rad/s)
Time 4	1.4255 degrees	1.2809 degrees	3.9288 degrees	0.0150(rad/s)	0.0160(rad/s)
Time 5	1.8358 degrees	1.3303 degrees	5.1121 degrees	0.0150(rad/s)	0.0144(rad/s)
Time 6	2.0327 degrees	1.1971 degrees	5.0959 degrees	0.0150(rad/s)	0.0144(rad/s)
Time 7	1.7938 degrees	1.1359 degrees	2.9685 degrees	0.0150(rad/s)	0.0147(rad/s)
Time 8	1.6378 degrees	1.1549 degrees	2.4473 degrees	0.0150(rad/s)	0.0148(rad/s)
Time 9	1.4014 degrees	0.9925 degrees	1.4444 degrees	0.0150(rad/s)	0.0149(rad/s)
Time 10	1.3316 degrees	1.1318 degrees	1.2701 degrees	0.0150(rad/s)	0.0150(rad/s)

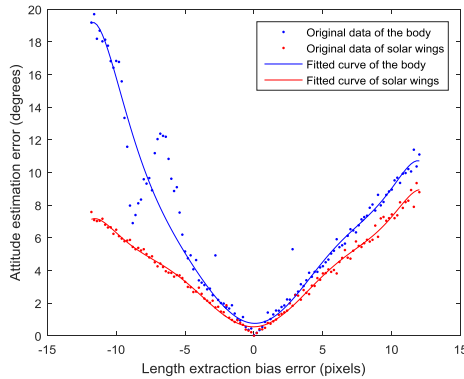


Fig. 12. Curves of estimation error change in different conditions of size feature extraction.

implemented ten times in each case, and the attitude estimation results are averaged to evaluate the accuracy of the target dynamic estimation. Fig. 12 illustrates the robustness of the proposed algorithm. Even when the bias error of size feature extraction reaches 5 pixels, the proposed algorithm ensures a 5° level estimation precision. In practical applications, it is feasible to control the feature extraction error under 5 pixels. Another experiential conclusion is summarized that the attitude estimation of the solar wing is always more accurate than the spacecraft body due to the difference of true sizes.

C. Dynamic Estimation of TG-I in Different Spin Patterns

1) *Observations of Target Spin Patterns Summarized From Public Studies of ENVISAT*: From relevant studies on the dynamic analysis of ENVISAT [2], [3], [9], [10], [15], the spin patterns of decommissioned satellites can be split into several stages. Before unexpected contact loss occurred, ENVISAT had maintained in a stabilized attitude condition so that the same part of the satellite (i.e., retroreflector panel) was always pointing toward a definite direction in orbit [2], [10]. In the early uncontrolled stage, observations from the FGAN Lab indicated that ENVISAT might make an inconstancy tumbling movement [10]. It is probably caused by the Earth's magnetic

and gravity fields. For the astrodynamics reason or the physical reason (called the gravitational stabilized reason), it verged to a spin motion, which was confirmed by a series of measured SLR data. However, the discussion about the rotation shaft did not come to an agreement. It seems that the rotation shaft is not constant but may have a regular motion according to long-term statistics.

2) *Dynamic Estimation of TG-I in Different Spin Patterns*: Drawing on the experience of observations in the previous section, we present four potential spin patterns to investigate the facility of the proposed algorithm in complex target spin conditions. The first one is the precession [34], which is described as the target is spinning around a definite rotation shaft at a constant rotation speed. The second condition evolves from the first, where the rotation shaft is fixed while the rotation speed varies. It is called the unstable precession in this article. The third is the nutation, which is common in the missile motion. In this case, beside the basic precession, the rotation shaft is also rotating around a definite nutation shaft. The last motion is the tumbling movement. It is simulated by the random changing of the rotation shaft and speed in the observation. It needs to be emphasized that this sort of tumbling motion is assumed to retain the planar spin during the single ISAR imaging period for the imaging requirement. In addition, the rotation speed of TG-I is set to be 0.015 rad/s and the rotation speed of the nutation shaft is set to be 0.005 rad/s in experiments after summarizing the public observation results of ENVISAT. The observation duration is set around 100 s corresponding to ten moments, and the size feature extraction error is set to 3 pixels in each experiment.

The target dynamic estimation results of these four motion patterns are listed in Tables IV–VII. In general, the attitude estimation errors of typical structures are controlled within 3° while the estimation result of the rotation speed is close to the true value at each moment. From the estimation results of the rotation shaft in Tables VI and VII, an experiential conclusion is drawn that the rotation of the spin shaft raises the estimation error of spin parameters. Theoretically, the proposed algorithm is performed independently at each moment without knowledge of the target spin pattern. Thus, the attitude parameter

TABLE V
ESTIMATION RESULTS OF THE UNSTABLE PRECESSION

Observation Time	Estimation Error of the Body	Estimation Error of the Solar Wing	Estimation Error of the Rotation Shaft	True value of the Rotation Speed	Estimation of the Rotation Speed
Time 1	1.8415 degrees	1.5126 degrees	3.0516 degrees	0.0107 (rad/s)	0.0113 (rad/s)
Time 2	1.2291 degrees	1.3641 degrees	2.0564 degrees	0.0210 (rad/s)	0.0200 (rad/s)
Time 3	1.3481 degrees	1.2218 degrees	4.0983 degrees	0.0150 (rad/s)	0.0139 (rad/s)
Time 4	1.3864 degrees	1.2585 degrees	3.9983 degrees	0.0154 (rad/s)	0.0143 (rad/s)
Time 5	1.5512 degrees	1.3158 degrees	4.7818 degrees	0.0091 (rad/s)	0.0095 (rad/s)
Time 6	2.0154 degrees	1.2149 degrees	3.6236 degrees	0.0213 (rad/s)	0.0219 (rad/s)
Time 7	1.8642 degrees	1.1341 degrees	2.4264 degrees	0.0206 (rad/s)	0.0209 (rad/s)
Time 8	1.6068 degrees	1.1312 degrees	1.8042 degrees	0.0194 (rad/s)	0.0195 (rad/s)
Time 9	1.2509 degrees	1.2152 degrees	0.8873 degrees	0.0220 (rad/s)	0.0220 (rad/s)
Time 10	1.3489 degrees	1.1025 degrees	1.2137 degrees	0.0203 (rad/s)	0.0204 (rad/s)

TABLE VI
ESTIMATION RESULTS OF THE NUTATION

Observation Time	Estimation Error of the Body	Estimation Error of the Solar Wing	Estimation Error of the Rotation Shaft	True value of the Rotation Speed	Estimation of the Rotation Speed
Time 1	1.6319 degrees	2.0210 degrees	0.8341 degrees	0.0150 (rad/s)	0.0153 (rad/s)
Time 2	1.2153 degrees	1.4309 degrees	2.0958 degrees	0.0150 (rad/s)	0.0158 (rad/s)
Time 3	1.4187 degrees	1.2844 degrees	4.2006 degrees	0.0150 (rad/s)	0.0161 (rad/s)
Time 4	1.3285 degrees	1.2691 degrees	3.9914 degrees	0.0150 (rad/s)	0.0161 (rad/s)
Time 5	2.0656 degrees	1.3326 degrees	8.2968 degrees	0.0150 (rad/s)	0.0144 (rad/s)
Time 6	2.3045 degrees	1.2161 degrees	7.7118 degrees	0.0150 (rad/s)	0.0146 (rad/s)
Time 7	2.1862 degrees	1.1091 degrees	5.9477 degrees	0.0150 (rad/s)	0.0151 (rad/s)
Time 8	2.1634 degrees	1.0799 degrees	5.4335 degrees	0.0150 (rad/s)	0.0153 (rad/s)
Time 9	2.3172 degrees	1.1018 degrees	5.1039 degrees	0.0150 (rad/s)	0.0156 (rad/s)
Time 10	2.5065 degrees	1.2238 degrees	5.2630 degrees	0.0150 (rad/s)	0.0156 (rad/s)

TABLE VII
ESTIMATION RESULTS OF THE TUMBLING MOTION

Observation Time	Estimation Error of the Body	Estimation Error of the Solar Wing	Estimation Error of the Rotation Shaft	True value of the Rotation Speed	Estimation of the Rotation Speed
Time 1	1.1990 degrees	1.5090 degrees	1.6641 degrees	0.0204 (rad/s)	0.0197 (rad/s)
Time 2	1.3262 degrees	1.1955 degrees	2.3060 degrees	0.0224 (rad/s)	0.0211 (rad/s)
Time 3	1.4767 degrees	1.2697 degrees	5.0092 degrees	0.0103 (rad/s)	0.0094 (rad/s)
Time 4	1.2631 degrees	1.2550 degrees	1.2774 degrees	0.0214 (rad/s)	0.0212 (rad/s)
Time 5	2.5539 degrees	1.1809 degrees	7.7449 degrees	0.0163 (rad/s)	0.0170 (rad/s)
Time 6	2.3484 degrees	1.2190 degrees	9.7307 degrees	0.0086 (rad/s)	0.0090 (rad/s)
Time 7	2.0985 degrees	0.9972 degrees	6.0999 degrees	0.0117 (rad/s)	0.0117 (rad/s)
Time 8	2.0438 degrees	1.0836 degrees	4.4809 degrees	0.0161 (rad/s)	0.0157 (rad/s)
Time 9	2.1852 degrees	1.0751 degrees	3.5384 degrees	0.0227 (rad/s)	0.0219 (rad/s)
Time 10	2.3937 degrees	1.1480 degrees	4.0706 degrees	0.0233 (rad/s)	0.0220 (rad/s)

of the rotation shaft ought to be estimated with similar precision among different spin patterns. However, a discrepant phenomenon has occurred, and it still can be explained by the imaging projection theory. In the case that the spin orientation of targets changes radically during the single imaging period,

the geometric manifold of the synthetic aperture is no longer a stabilized plane. As a result, the conventional turntable model does not coincide with the observation echo data, and the high-resolution imaging cannot be ensured in this circumstance. Thus, the two-step optimization of the target

motion state is built in a biased manner, which causes the estimation error. However, it is not a drawback of the proposed algorithm. A basic premise of the proposed algorithm is stable and high-resolution imaging for the spacecraft. Inferred from the measured imagery published by the FGAN Lab (Available at <https://www.fhr.fraunhofer.de/tiangong-bilder>), the well focusing performance of the images proves that the rotation shaft of TG-I seems to be changing continuously in the radar imagery sequence. Therefore, we believe the premise of high-resolution imagery for spin targets is satisfied in most practical applications.

V. CONCLUSION

In this article, in order to estimate the dynamic parameters of spin spacecraft, an approach is presented based on multiple-station ISAR images. With the development of the geometric projection of ISAR multiple-station observations, an explicit expression is derived bridging the RD imagery and the spin motion of the target. Based on the prior size knowledge of typical structures, target dynamic parameters are determined in a two-step optimization with the accommodation of CGOA. The experimental results have confirmed the effectiveness of the proposed algorithm in different target spin patterns, and a self-verification approach is also proposed to evaluate the estimation results. Compared with the existing methods, the proposed method can eliminate its dependence on long-time historical data collections and depended on the interpretation of synchronous multiple-station ISAR images entirely. We believe this article provides an effective approach to accomplishing dynamic estimation of spin targets in orbit. However, it is still a challenge to estimate the dynamic parameters of the space debris which tumbles at a high speed.

ACKNOWLEDGMENT

The authors would like to thank the anonymous reviewers for their valuable comments to improve the article.

REFERENCES

- [1] J. Tang, L. Liu, H. Cheng, S. Hu, and J. Duan, "Long-term orbit prediction for Tiangong-1 spacecraft using the mean atmosphere model," *Space Res.*, vol. 55, no. 5, pp. 1432–1444, 2015.
- [2] D. Kucharski *et al.*, "Attitude and spin period of space debris Envisat measured by satellite laser ranging," *IEEE Trans. Geosci. Remote Sens.*, vol. 52, no. 12, pp. 7651–7657, Dec. 2014.
- [3] N. Koshkin, E. Korobeynikova, L. Shkun, S. Strakhova, and Z. H. Tang, "Remote sensing of the EnviSat and Cbers-2B satellites rotation around the centre of mass by photometry," *Adv. Space Res.*, vol. 58, no. 3, pp. 358–371, 2016.
- [4] L. Carozza and A. Bevilacqua, "Error analysis attitude determination using a vision-based approach," *ISPRS J. Photogram. Remote Sens.*, vol. 83, pp. 19–29, 2013, doi: 10.1016/j.isprsjprs.2013.05.007.
- [5] T. Kouyama, A. Kanemura, S. Kato, N. Imamoglu, T. Fukuhara, and R. Nakamura, "Satellite attitude determination and map projection based on robust image matching," *Remote Sens.*, vol. 9, no. 1, p. 90, 2017.
- [6] G. Kirchner, W. Hausleitner, and E. Cristea, "Aisai spin parameter determination using Graz kilohertz satellite laser ranging data," *IEEE Trans. Geosci. Remote Sens.*, vol. 45, no. 1, pp. 201–205, Jan. 2007.
- [7] G. Kirchner, D. Kucharski, and E. Cristea, "Gravity probe-B: New methods to determine spin parameters from kHz SLR data," *IEEE Trans. Geosci. Remote Sens.*, vol. 47, no. 1, pp. 370–375, Jan. 2009.
- [8] N. Gomez and S. Walker, "Earth's gravity gradient and eddy currents effects on the rotational dynamics of space debris objects: Envisat case study," *Adv. Space Res.*, vol. 56, no. 3, pp. 494–508, 2015.
- [9] J. Pittet, J. Silha, and T. Schildknecht, "Spin motion determination of the Envisat satellite through laser ranging measurements from a single pass measured by a single station," *Adv. Space Res.*, vol. 61, no. 4, pp. 1121–1131, 2018.
- [10] S. Sommer, J. Rosebrock, D. Cerutti-Maori, and L. Leushacke, "Temporal analysis of Envisat's rotational motion," in *Proc. Eur. Conf. Space Debris*, 2017.
- [11] K. Suwa, T. Wakayama, and M. Iwamoto, "Three-dimensional target geometry and target motion estimation method using multistatic ISAR movies and its performance," *IEEE Trans. Geosci. Remote Sens.*, vol. 49, no. 6, pp. 2361–2373, Jun. 2011.
- [12] Y. Zhou, L. Zhang, Y. Cao, and Z. Wu, "Attitude estimation and geometry reconstruction of satellite targets based on ISAR image sequence interpretation," *IEEE Trans. Aerosp. Electron. Syst.*, vol. 55, no. 4, pp. 1698–1711, Aug. 2019.
- [13] S. Saremi, S. Mirjalili, and A. Lewis, "Grasshopper optimisation algorithm: Theory and application," *Adv. Eng. Softw.*, vol. 105, pp. 30–47, 2017, doi: 10.1016/j.advengsoft.2017.01.004.
- [14] S. Arora and P. Anand, "Chaotic grasshopper optimization algorithm for global optimization," *Neural Comput. Appl.*, vol. 31, no. 8, pp. 4385–4405, 2019.
- [15] H. Lin and C. Zhao, "An estimation of Envisat's rotational state accounting for the precession of its rotational axis caused by gravity-gradient torque," *Adv. Space Res.*, vol. 61, no. 1, pp. 182–188, 2018.
- [16] ARINC Research Corporation. *Navstar GPS Space Segment*. Accessed: Jan. 14, 2003. [Online]. Available: <http://www.navcen.uscg.gov/pubs/gps/icd200/default>
- [17] C. Rino. *Satellite Orbit Computation*. Accessed: Sep. 30, 2010. [Online]. Available: <http://www.mathworks.com/matlabcentral/leexchange/28888-satellite-orbit-computation>
- [18] K. Birch and M. Downs, "An updated Edlen equation for the refractive index of air," *Metrologia*, vol. 30, no. 3, pp. 155–162, 1993.
- [19] M. Wang, Y. Zhu, S. Jin, J. Pan, and Q. Zhu, "Correction of ZY-3 image distortion caused by satellite jitter via virtual steady reimaging using attitude data," *ISPRS J. Photogram. Remote Sens.*, vol. 119, pp. 108–123, Sep. 2016.
- [20] J. T. Mayhan, M. L. Burrows, K. M. Cuomo, and J. E. Piou, "High resolution 3D 'snapshot' ISAR imaging and feature extraction," *IEEE Trans. Aerosp. Electron. Syst.*, vol. 37, no. 2, pp. 630–642, Apr. 2001.
- [21] L. Zhang, Z.-J. Qiao, M. Xing, Y. Li, and Z. Bao, "High-resolution ISAR imaging with sparse stepped-frequency waveforms," *IEEE Trans. Geosci. Remote Sens.*, vol. 49, no. 11, pp. 4630–4651, Nov. 2011.
- [22] L. Zhang *et al.*, "Resolution enhancement for inversed synthetic aperture radar imaging under low SNR via improved compressive sensing," *IEEE Trans. Geosci. Remote Sens.*, vol. 48, no. 10, pp. 3824–3838, Oct. 2010.
- [23] X. Xu and R. Narayanan, "Three-dimensional interferometric ISAR imaging for target scattering diagnosis and modeling," *IEEE Trans. Image Process.*, vol. 10, no. 7, pp. 1094–1102, Jul. 2001.
- [24] A. F. Garcia-Fernandez, O. A. Yeste-Ojeda, and J. Grajal, "Facet model of moving targets for ISAR imaging and radar back-scattering simulation," *IEEE Trans. Aerosp. Electron. Syst.*, vol. 46, no. 3, pp. 1455–1467, Jul. 2010.
- [25] F. Wang, T. F. Eibert, and Y. Q. Jin, "Simulation of ISAR imaging for a space target and reconstruction under sparse sampling via compressed sensing," *IEEE Trans. Geosci. Remote Sens.*, vol. 53, no. 6, pp. 3432–3441, Jun. 2015.
- [26] A. Boag, "A fast physical optics (FPO) algorithm for high frequency scattering," *IEEE Trans. Antennas Propag.*, vol. 52, no. 1, pp. 197–204, Jan. 2004.
- [27] FGAN Lab. (Mar. 2018). *Forscher des Fraunhofer FHR Begleiten Wiedereintritt der Chinesischen Raumstation Tiangong-1*. [Online]. Available: <https://www.fhr.fraunhofer.de/tiangong-bilder>
- [28] R. Gonzales and R. Woods, *Digital Image Processing*. Beijing, China: Publishing House of Electronics Industry, 2007, pp. 432–435.
- [29] S. Deans, *The Radon Transform and Some of Its Applications*. North Chelmsford, MA, USA: Courier Corporation, 2007.
- [30] I. Fogel and D. Sagi, "Gabor filters as texture discriminator," *Biological*, vol. 61, no. 2, pp. 103–113, 1989.
- [31] S. Reis and K. Tasdemir, "Identification of hazelnut fields using spectral and Gabor textural features," *ISPRS J. Photogram. Remote Sens.*, vol. 66, no. 5, pp. 652–661, 2011.
- [32] J. Wu *et al.*, "Distributed trajectory optimization for multiple solar-powered UAVs target tracking in urban environment by adaptive grasshopper optimization algorithm," *Aerosp. Sci. Technol.*, vol. 70, pp. 497–510, Nov. 2017.

- [33] H. Lu, X. Wang, Z. Fei, and M. Qiu, "The effects of using chaotic map on improving the performance of multiobjective evolutionary algorithms," *Math. Problems Eng.*, vol. 2014, Feb. 2014, Art. no. 924652.
- [34] L. Hong, F. Dai, and H. Liu, "Motion-parameter estimation for precession-with-nutation space targets based on wideband radar measurements," *IEEE Trans. Aerosp. Electron. Syst.*, vol. 52, no. 2, pp. 643–657, Apr. 2016.



Lei Zhang was born in Zhejiang, China, in 1984. He received the Ph.D. degree from Xidian University, Xian, China, in 2012.

He is currently an Associate Professor with the School of Electronics and Communication Engineering, Sun Yat-sen University, Guangzhou, China. His research interests are radar imaging [synthetic aperture radar (SAR)/inverse SAR (ISAR)] and motion compensation.



Yejian Zhou was born in Zhejiang, China, in 1993. He received the B.S. degree in electronic engineering from Xidian University, Xian, China, in 2015, where he is currently pursuing the Ph.D. degree in signal processing with the National Laboratory of Radar Signal Processing. He is also studying as a visiting Ph.D. student in the Department of Urban Planning and Environment, KTH Royal Institute of Technology, Stockholm, Sweden.

His research interests include ISAR imaging and image interpretation.



Yunhe Cao was born in Anhui, China. He received the B.S., M.S., and Ph.D. degrees from Xidian University, Xian, China, in 2001, 2004, and 2006, respectively.

He is currently a Professor with the National Laboratory of Radar Signal Processing, Xidian University. His research interests include MIMO radar, digital array radar, adaptive signal processing, and target detection.